

<https://doi.org/10.1038/s42005-025-02218-7>

# Acoustic higher-order topological insulator from momentum-space nonsymmorphic symmetries

Check for updates

Jinbing Hu<sup>1,2</sup>✉, Tianle Song<sup>1</sup>, Kai Zhou<sup>1</sup>, Xuntao Jiang<sup>3</sup>, Songlin Zhuang<sup>1</sup> & Yi Yang<sup>1,2</sup>✉

Momentum-space nonsymmorphic symmetries, stemming from the projective algebra of synthetic gauge fields, can modify the manifold of the Brillouin zone and lead to a variety of topological phenomena. Recently, higher-order topological insulators (HOTIs) are predicted to be stabilized by these symmetries but call for experimental confirmation. We present an acoustic realization of HOTIs protected by a pair of anticommutative momentum-space glide reflections. We confirm the presence of momentum-space glide reflection from the measured momentum half translation of edge bands and their momentum-resolved probability distribution using a cylinder geometry made of acoustic resonator arrays. In particular, we observe both intrinsic and extrinsic HOTI features in such a cylinder: hopping strength variation along the open boundary leads to a bulk gap closure, while that along the closed boundary results in an edge gap closure. In addition, we confirm the presence of quadrupole corner modes with transmission and field distribution measurements. Our observation enriches the study of topological physics of momentum-space nonsymmorphic symmetries.

Projective symmetries have recently been shown to give rise to intriguing topological phenomena<sup>1–13</sup>. The presence of synthetic gauge fields projectively modifies the form of conventional symmetries, such as translation and reflection symmetries, and their associated symmetry algebra, which can protect Möbius edge modes<sup>9–11</sup> and Klein-bottle topological insulators and semimetals<sup>14–17</sup>. One particular kind of projective symmetry is the momentum-space nonsymmorphic ( $\mathbf{k}$ –NS) reflection, which besides flipping the sign of a momentum, also performs a half translation along the reflection plane<sup>14,15,18</sup>. This momentum-space glide reflection operation is complementary but different from its real-space counterparts that have been extensively studied for stabilizing topological insulators and semimetals<sup>19–24</sup>. The addition of half translation in  $\mathbf{k}$ –NS reflection has several consequences. First, the half translation removes the reflection axis and transforms the conventional reflection into a free operator that can modify the manifold of Brillouin zone (BZ) from a torus into a Klein bottle<sup>14</sup>. Second, due to the non-orientability of Brillouin zone,  $\mathbf{k}$ –NS reflection can also protect topological Weyl semimetals that obey a no-go theorem<sup>25</sup> that is distinct from its counterpart for Weyl semimetals on the Brillouin torus<sup>26–29</sup>. Third,  $\mathbf{k}$ –NS reflection constrains bulk polarization and Wannier-sector polarization nonlocally, and a pair of anti-commutative  $\mathbf{k}$ –NS reflection can further stabilize intrinsic higher-order topological insulators (HOTIs) on a real projective plane<sup>30</sup>.

By generalizing the electric dipole moment<sup>31–33</sup> to higher electric multipole moments, higher-order topological insulators (HOTIs) were recently defined<sup>34–36</sup> and experimentally demonstrated in various physical platforms (e.g., refs. 37–43). According to whether the phase transition is related to bulk gap closure or not, HOTIs are ramified into intrinsic and extrinsic ones<sup>44–46</sup> that are respectively featured with symmetry-protected topological phase (SPTP) and boundary-obstructed topological phase (BOTP)<sup>44,47,48</sup>. In previous HOTI studies, SPTP and BOTP are typically considered mutually exclusive to each other once a model is constructed; nevertheless, it was recently predicted that in a HOTI protected by  $\mathbf{k}$ –NS reflections, BOTP could appear *within* the interior of an SPTP<sup>30</sup>. Despite that higher-order topological insulators stabilized by projective translation and reflection symmetries have been observed<sup>15,49</sup>, the occurrence of boundary obstruction within an SPTP, together with the associated characterization of  $\mathbf{k}$ –NS glide reflection from boundary features, has not been experimentally demonstrated.

In this work, we realize a HOTI protected by a pair of anticommutative momentum-space glide reflections. Based on acoustic resonator array structures, we confirm the realization of  $\mathbf{k}$ –NS glide reflection from the momentum-resolved probability density of edge bands on a cylinder geometry, demonstrate the appearance of boundary obstruction within the interior of an SPTP, and observe the associated corner modes stabilized by  $\mathbf{k}$

<sup>1</sup>School of Optical-Electrical and Computer Engineering, University of Shanghai for Science and Technology, Shanghai, China. <sup>2</sup>Department of Physics and HK Institute of Quantum Science and Technology, The University of Hong Kong, Pokfulam, Hong Kong, China. <sup>3</sup>Shanghai Szon Mechanical & Electrical Technology Co. Ltd, Shanghai, China. ✉e-mail: [hujinbing@usst.edu.cn](mailto:hujinbing@usst.edu.cn); [yiyg@hku.hk](mailto:yiyg@hku.hk)

—NS glide reflections. Acoustic resonator array structures are fabricated into two geometries: a planar full open structure for observing bulk, edge, and corner modes and a cylinder, which preserves the  $\mathbf{k}$ —NS reflection along its periodic direction. The measured edge bands reveal a momentum half translation between the edge modes localized at the opposite ends of the sample, which is also verified by their momentum-resolved probability density. Furthermore, we observe both BOTP and SPTP phase transitions, respectively, by changing the intracell coupling strength along either the closed or open boundaries of the cylinder structure.

## Results

### Model construction

The basic building blocks of the system are shown in Fig. 1a. Due to the presence of  $\pi$  gauge flux, the conventional reflection  $m_x$  ( $m_y$ ) is projectively modified as  $M_x = U\mathcal{L}_{G_x/2}m_x$  ( $M_y = V\mathcal{L}_{G_y/2}m_y$ ), where  $U(V)$  is a unitary matrix whose concrete form is strongly related to the connection configuration (see Supplementary Fig. 1 of Supplementary Note 1 for details), and  $\mathcal{L}_{G_i/2}$  ( $i = x, y$ ) denotes the half translation along  $i$  axis<sup>14</sup>. We construct the square lattice model with a checkerboard  $\pi$  flux pattern (Fig. 1b), which is featured with both  $\mathbf{k}$ —NS  $M_x$  and  $M_y$ <sup>30</sup>. The simultaneous presence of  $M_x$  and  $M_y$  naturally defines  $\mathbf{k}$ —NS  $P_\pi \equiv M_x M_y$ , that is featured with a half translation along both  $x$  and  $y$  directions. Interesting,  $M_x$ ,  $M_y$ , and  $P_\pi$  jointly divide the first BZ into four real projective plane ( $\mathbb{RP}^2$ ) manifolds (see Supplementary Fig. 2 of Supplementary Note 2), each of which is capable of diagnosing system topological feature<sup>30</sup>. The associated Bloch Hamiltonian is

$$H(k_x, k_y) = \begin{pmatrix} 0 & a_+ & b_+ & 0 \\ a_+^* & 0 & 0 & b_- \\ b_+^* & 0 & 0 & a_- \\ 0 & b_-^* & a_-^* & 0 \end{pmatrix}, \quad (1)$$

with  $a_\pm = \gamma_x \pm \lambda_x e^{-ik_x}$ ,  $b_\pm = \pm \gamma_y + \lambda_y e^{-ik_y}$ , and  $*$  denoting complex conjugate. Here,  $\gamma_x$  and  $\gamma_y$  ( $\lambda_x$  and  $\lambda_y$ ) represent the intra-cell (inter-cell) hopping amplitudes along  $x$  and  $y$ , respectively. Without loss of generality, we set unity lattice constants and  $\lambda_x = \lambda_y = 1$ . For the chosen coupling arrangement in Fig. 1b, the  $\mathbf{k}$ —NS  $M_x$  and  $M_y$  have the form:  $M_x = \sigma_3 \otimes \tau_1$ ,  $M_y = \sigma_1 \otimes \tau_0$ ,  $P_\pi = i\sigma_2 \otimes \tau_1$ , where  $\sigma$ 's and  $\tau$ 's are Pauli matrices acting on sites along  $y$  and  $x$ , respectively. The gauge flux pattern in Fig. 1b enables the anti-commutativity of  $M_x$  and  $M_y$ , which together stabilize an intrinsic higher-order topological phase manifested by a nontrivial quadrupole moment, corner modes, and bulk gap closing across the phase boundary<sup>30</sup>. Different from their conventional counterparts,  $\mathbf{k}$ —NS  $M_x$ ,  $M_y$  and  $P_\pi$

exhibit nonlocal constraints to bulk polarization and wannier-sector polarization due to the presence of half translation (see Supplementary Note 3 for details). Aside from Fig. 1b, there exists a complementary way to insert a checkerboard  $\pi$  flux pattern in the square lattice<sup>50,51</sup>, which also generates a pair of  $\mathbf{k}$ —NS  $M_x$  and  $M_y$ ; however, in that case, the  $\mathbf{k}$ —NS  $M_x$  and  $M_y$  are commutative and the quadrupole moment is trivial (see Supplementary Fig. 4 in Supplementary Note 5).

### Sample design

In the experiment, the checkerboard  $\pi$  flux pattern in Fig. 1b is implemented via coupled acoustic resonator structures<sup>4,10,30,41</sup>, where the resonators emulating the lattice site are designed to work at the dipolar mode near frequency 8587 Hz (see Supplementary Fig. 5 in Supplementary Note 6). By perpendicularly arranging two identical resonators, the hopping phase of these two identical resonators is controllable through left or right localizing the connecting tube<sup>4,10,41</sup>. The coupling strength can be tuned via the width of the cross-section of the tube and its position with respect to the center of the resonator.

In addition to the full-open planar structures for corner mode characterizations, here we also implement cylinder structures (open and closed on two directions, respectively, see Fig. 1c) to experimentally validate the momentum half translation of the  $\mathbf{k}$ —NS reflection. For this aim, two types of connections among resonators should be designed as equivalent: along the open  $y$  direction, there is a planar connection where the two neighboring resonators and the connecting tube are co-planar, and along the closed  $x$  direction, there is a curved connection, where the two neighboring resonators are connected via a curved tube described by a parametric angle  $\theta$  (see inset of Fig. 1c). The design challenge is that despite linked with distinct planar and curved connections, the resonators should maintain the periodicity and the same pressure distribution along both directions (see Supplementary Fig. 5 in Supplementary Note 6), such that the fabricated cylinder can faithfully realize the Hamiltonian [Eq. (1)] in its cylinder geometry. To this end, we optimize the geometry of the resonators and their connections and arrive at the set of parameters (Fig. 1b):  $a = 5.2$  mm,  $b = 10$  mm,  $c = 20$  mm, and the connections with  $\theta = 0$  and  $\theta = \pi/16$  are equivalent for tube width  $d$  in the range of 1–4.5 mm when the tube length is fixed at 9.3 mm, as shown in Fig. 1d. Unless noted otherwise, the simulation model and realistic sample are fabricated based on the optimization above. Figure 1d also shows that the central frequency of resonators is designed to be uniform under various tube length such that we can unify the on-site potential of resonators.

### Half translation of $\mathbf{k}$ —NS reflection

We validate the  $\mathbf{k}$ —NS reflection symmetry using a  $y$ -open cylinder (Fig. 2a). In this cylinder, because the translation symmetry along  $x$  remains

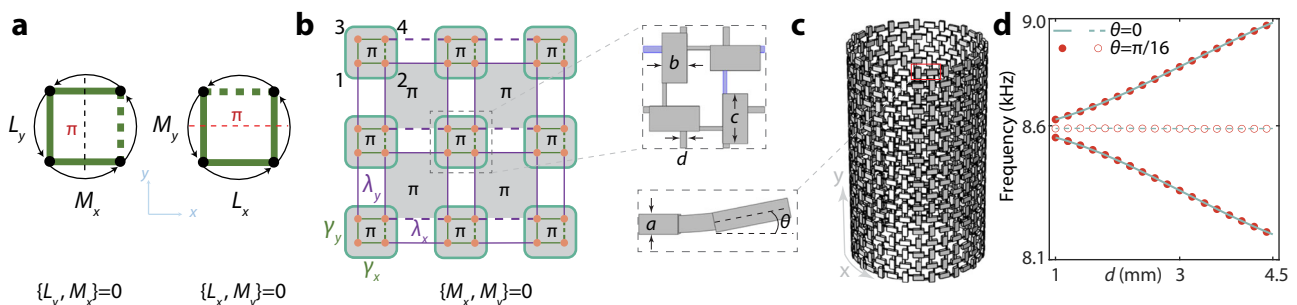


**Fig. 1 | Lattice model featuring nonsymmorphic reflections in momentum space and its acoustic realization.** **a** Threading  $\pi$  flux projectively modifies the conventional reflections  $m_i$  ( $i = x, y$ ) into  $\mathbf{k}$ —NS ones  $M_i$  ( $i = x, y$ ), which anticommute with the translation symmetry  $L_j$  ( $j = y, x$ ) along the other direction. **b** Model with checkerboard  $\pi$  flux enables anti-commutative  $M_x$  and  $M_y$ . Solid and dashed lines indicate positive and negative real hoppings hoppings, respectively. The inset displays the implementation of an acoustic lattice unit cell, where blue (gray) tubes indicate negative (positive) hoppings. **c** A cylinder structure of the lattice model

preserves the translation symmetry in  $x$  direction, thus, in turn, obeys  $\mathbf{k}$ —NS  $M_y$ . The inset shows the bending design of the resonator connection along the  $x$  direction, where  $\theta$  is the bending angle. **d** The splitting frequencies of two perpendicularly arranged identical resonators as a function of tube width  $d$  for  $\theta = 0$  (green lines) and  $\theta = \pi/16$  (red solid circles), respectively. In the middle, the near horizontal dashed line and hollow circles are the averages of the split frequencies, which indicate that the on-site potentials of resonators in both curved and planar connections are uniform with little variation under tube width changes.

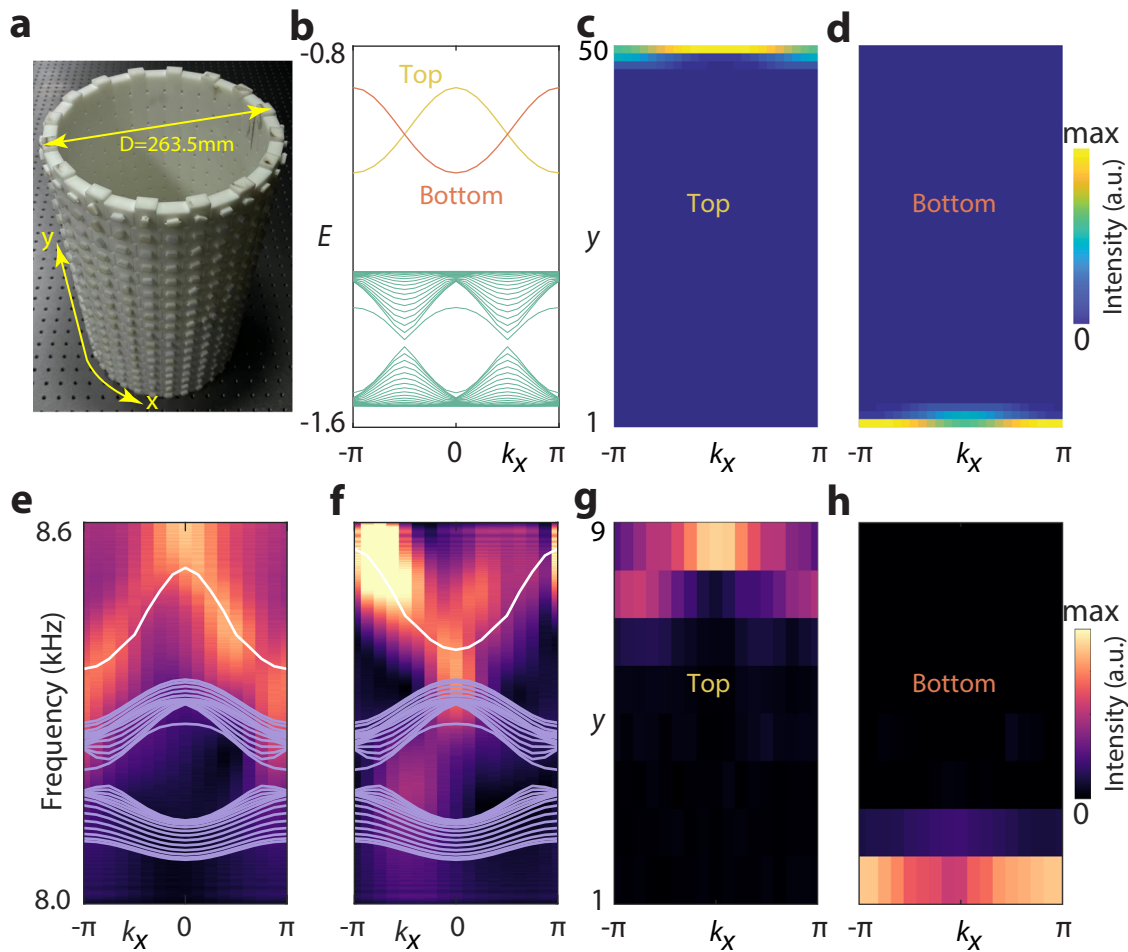


**Fig. 2 | Measured edge bands and their momentum-resolved probability density on an acoustic cylinder.** **a** Photo of the cylinder with the size of  $16 \times 9$  unit cells along  $x$  and  $y$  respectively. The connecting tube widths of the cylinder along  $x$  and  $y$  axes are:  $d_{\text{intra}}^x = 1.7$  mm,  $d_{\text{inter}}^x = 3.0$  mm,  $d_{\text{intra}}^y = 1.7$  mm,  $d_{\text{inter}}^y = 4.5$  mm. **b** Projected bands of the  $y$ -open cylinder with hopping parameters  $\gamma_x = \gamma_y = 0.1$ ,  $\lambda_x = \lambda_y = 1.0$ . **c, d** The momentum-resolved probability density of edge bands in **(b)**.

25 unit cells are assumed along the  $y$  axis. **e, f** Measured edge bands of the acoustic cylinder under different source conditions. The source is positioned at the top **(e)** and bottom **(f)** edge of the cylinder, respectively. The purple and white curves are the theoretical bulk and edge bands from acoustic full-wave simulations. **g, h** Measured momentum-resolved probability density of the edge bands (corresponding to white curves in **(e, f)**, respectively).

intact,  $\mathbf{k}-\text{NS}M_y$  is preserved and pairs both bulk and edge bands with their half-translation partners. Detached from the bulk bands (see Fig. 2b), the top-localized and bottom-localized edge bands (red and yellow curves in Fig. 2b) have the same dispersion relation but differ by a half translation, which serves as a convenient observable to confirm the existence of  $\mathbf{k}-\text{NS}$  reflection. This half translation of  $\mathbf{k}-\text{NS}M_y$  is also manifested through the predicted momentum-resolved probability density of edge bands, as shown by the comparison of Fig. 2c, d.

Experimentally, an acoustic cylinder with the size of  $16 \times 9$  unit cells along  $x$  and  $y$  direction, respectively, is fabricated (see Fig. 2a). To measure the top-localized and bottom-localized edge bands, we excite the cylinder with a broadband sound source localized at the top or bottom resonator, and simultaneously record the time-domain signal from the same resonators at each cell. By Fourier transform on the recorded time-space data (see Supplementary Note 7 for details), the dispersion of the measured top and bottom edge bands is obtained, as shown by the hot maps in Fig. 2e, f, where the discrete curves are simulation results. The measured edge bands agree well with the theoretical ones (white lines) in the simulation, both of which exhibit momentum half translation between the top and bottom edge bands. The inhomogeneous distribution of Fourier intensity in Fig. 2f may come from the fabrication tolerance (see Supplementary Note 8 for details). In addition, the momentum-resolved probability density of the top and bottom edge bands are also measured by scanning the detector (position fixed at the

same resonator with each unit cell) across the whole cylinder (see Supplementary Fig. 7 in Supplementary Note 7), and the results are plotted in Figs. 2g and h, which also verify the half translation between these two edge bands.

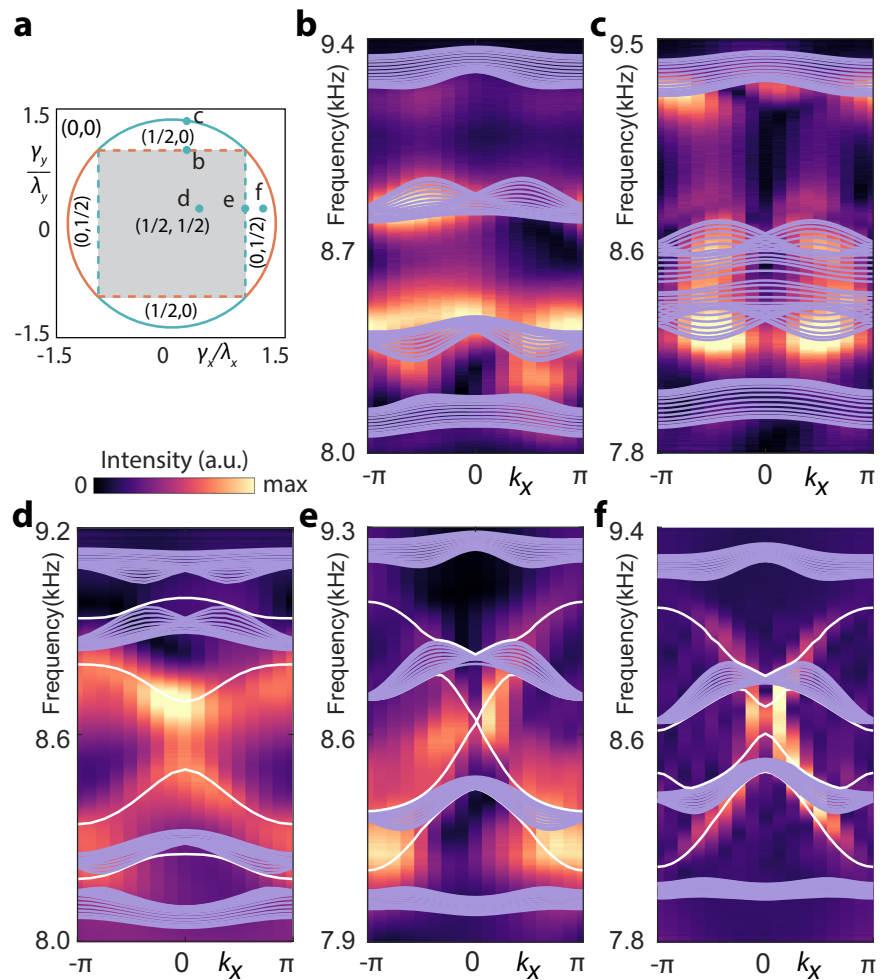
### BOTP inside SPTP

As predicted in ref. 30, boundary obstruction can appear within the interior of SPTP for HOTIs stabilized by  $\mathbf{k}-\text{NS}$  symmetries. In model Fig. 1b, BOTP can be introduced inside the intrinsic quadrupole phase by opening one pair of boundaries. Figure 3a shows the phase diagram of edge polarization<sup>34,35</sup> (see Supplementary Note 4 for computation method) of model Fig. 1b in cylinder geometry, where the phase transition can occur via either bulk or edge gap closures: hopping strength variation along the *open* direction leads to a *bulk* gap closure (Fig. 3b, c that cross a solid arc in Fig. 3a), while that along the *periodic* direction results in an *edge* gap closure (see Fig. 3d–f that cross a dashed line in Fig. 3a).

We demonstrate such BOTP and SPTP transitions by measuring the band structures under various coupling strengths along the closed and open directions of the fabricated acoustic cylinders, respectively. In Fig. 3b–f, the measured results are plotted overlaid with theoretical bands (discrete curves; edge modes in white and bulk modes in purple) of  $y$ -open cylinder structures. When  $d_{\text{intra}}^y = d_{\text{inter}}^y$  the bulk bands exhibit a large gap (Fig. 3b), which closes as we increase  $d_{\text{intra}}^y$  (Fig. 3c), indicating the occurrence of SPTP

**Fig. 3 | Boundary-obstructed topological phase and symmetry-protected topological phase transitions along the closed and open boundaries.**

**a** Phase diagram of edge polarization ( $p_x^e, p_y^e$ ). Red and green lines correspond to  $x$ -open and  $y$ -open cylinders, respectively. Solid and dashed lines refer to bulk and edge gap closure, respectively. **b–f** Measured band structure of the  $y$ -open acoustic cylinder with structure parameters indicated by their associated points in **a**. The purple and white curves are the theoretical bulk and edge bands from acoustic full-wave simulations. The bulk gap closure from **(b)** to **(c)** indicates the symmetry-protected topological phase transition of edge polarization along the open boundary. The edge band gap closes and reopens in **(d–f)**, indicating the boundary-obstructed topological phase transition of edge polarization along the closed boundary. The structural parameters for the  $y$ -open acoustic cylinder are  $d_{\text{intra}}^x = (1.7, 1.7, 1.7, 3.0, 3.5)$  mm,  $d_{\text{inter}}^x = (4.5, 4.5, 3.0, 3.0, 3.0)$  mm,  $d_{\text{intra}}^y = (3.0, 4.0, 1.7, 1.7, 1.7)$  mm,  $d_{\text{inter}}^y = (3.0, 3.0, 4.5, 4.5, 4.5)$  mm for **(b–f)**, respectively.



transition. In contrast, the scenario along closed boundary (i.e.,  $x$  axis) is different. When  $d_{\text{intra}}^x < d_{\text{inter}}^x$ , a large edge band gap is observed, (Fig. 3d), which closes when  $d_{\text{intra}}^x = d_{\text{inter}}^x$  (Fig. 3e) and reopens once  $d_{\text{intra}}^x$  exceeds  $d_{\text{inter}}^x$  (Fig. 3f). Jointly, Fig. 3d–f display the process of BOTP transition.

### Measurement of corner modes

The bulk of the model in Fig. 1b exhibits a quadrupole insulating phase<sup>23,52–55</sup>, which is manifested by gapped corner modes under full open boundary condition when  $|\gamma_x| < |\lambda_x|$  and  $|\gamma_y| < |\lambda_y|$ <sup>30</sup>. Based on the building block in Fig. 1, we fabricate the planar acoustic sample with a size of  $7 \times 7$  unit cells via 3D printing technique. For the scanning of the sound field, each resonator is perforated with a hole (which is sealed when not used) to insert the sound source or microphone. The experiment setup for spectra measurement is shown in Fig. 4a, where the acoustic source and microphone are localized in the bulk of the sample with two resonators in between; the source and microphone will be located at the edge or corner of the sample when the edge or corner spectra are measured. The details of the source-detector configurations for the bulk, edge, and corner spectra can be found in Supplementary Note 7. As shown in Fig. 4c, the bulk (yellow dots) and edge (red dots) spectra feature a common wide gap at 8400–8860 Hz, at the center of which a corner (green dots) spectral peak (around 8596 Hz) appears. The corresponding simulation results are plotted in Fig. 4b, in good agreement with the measured spectra. Note that the measured spectra in Fig. 4c are normalized with respect to their respective maximum values, and the asymmetries in bulk and edge spectra may arise from the fact that the local density of states have different spatial dependence for different bulk, edge, and corner eigenmodes within the unit cell. The field distributions at the specific peak frequencies of bulk, edge, and corner spectra, i.e., 8042 Hz,

9006 Hz, 8595 Hz, respectively, are measured by field scanning across all resonators. The results are displayed in Fig. 4d–f, and are in good agreement with the associated numerical simulations (Fig. 4g–i) under the same excitation frequencies (see Supplementary Note 9 for the measurement details of the pressure distribution). In addition, we also measured the transmission spectrum of corner mode with one resonator nearby the corner being filled with a plasticine defect, under which the spectra and corner mode exhibit robustness (see Supplementary Fig. 9 in Supplementary Note 10).

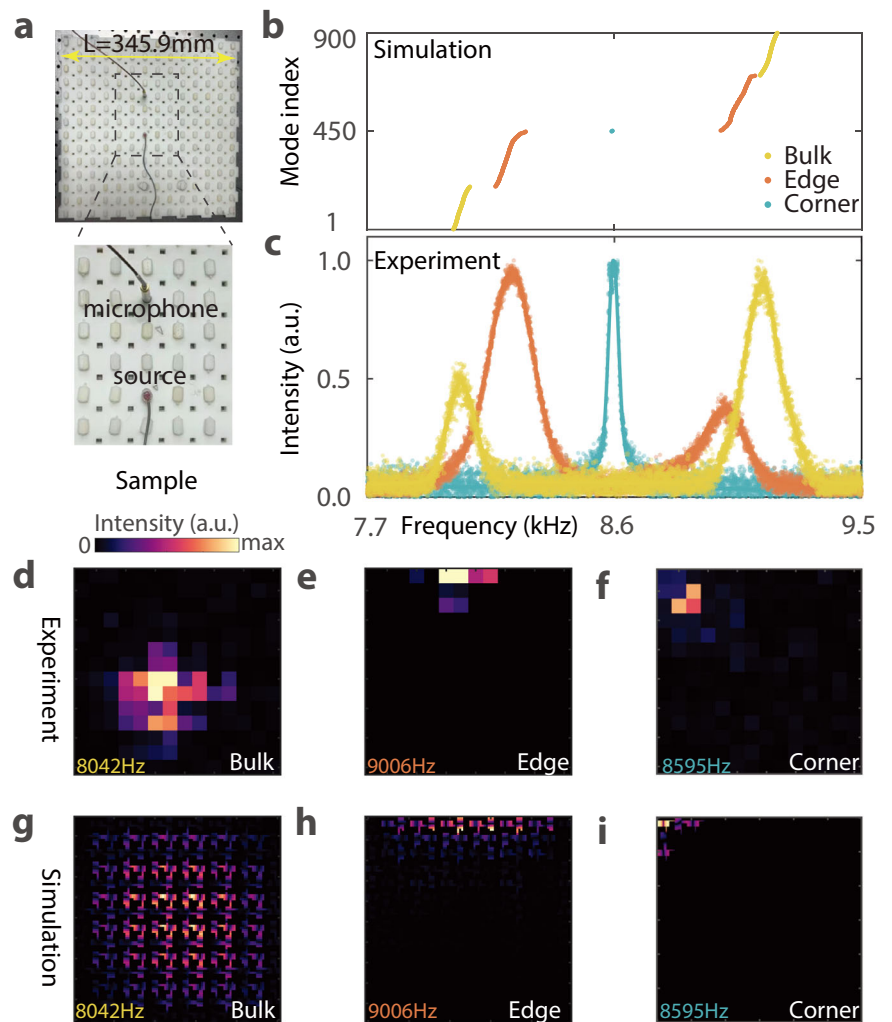
### Conclusions

In summary, we experimentally realized a pair of momentum-space glide reflections that protect a higher-order topological insulating phase in an acoustic resonator array. We observed the momentum half translation of the symmetry, the boundary obstruction within a symmetry-protected phase, and the resulting quadrupole corner modes. Aside from the acoustic realization here, the  $\text{RP}^2$  BZ and its HOTIs stabilized by momentum-space nonsymmorphic symmetries can be implemented in diverse physical platforms, such as coupled resonator optical waveguides, mechanical metamaterials, electric circuits, and synthetical frequency dimensions. The findings here could be relevant for a wider range of momentum-space nonsymmorphic symmetries that can be flexibly synthesized from inhomogeneous gauge fields in both Hermitian and non-Hermitian systems.

### Methods

All the acoustic design and simulations were performed using the pressure acoustic module in COMSOL Multiphysics—a commercial software. Among these simulations, the air density and sound speed are respectively set as  $\rho = 1.29 \text{ kg/m}^3$  and  $\nu = 343.5 \text{ m/s}$ , and all the boundaries of acoustic

**Fig. 4 | Corner mode measurement.** **a** Setup for measuring the spectral response. The inset is a zoom-in for better showing the source-detector positioning of the sound source and the probing microphone. Simulated (**b**) and measured (**c**) spectra of bulk (yellow), edge (brown), and corner (green) modes. Measured (**d–f**) and simulated (**g–i**) pressure intensity distributions for bulk, edge, and corner modes with frequencies being 8042 Hz, 9006 Hz, and 8595 Hz, respectively.



resonators are set as sound hard boundary. The photosensitive resin material used for fabrication is of the type R4600 with Hardness 145 (ASTM D 2240), which can be taken as acoustically rigid in the airborne sound environment, given the extremely mismatched acoustic impedance between resin and air. The samples were fabricated by company ([www.wenext.cn](http://www.wenext.cn)) with fabrication resolution 0.1 mm.

To faithfully realize the Hamiltonian [Eq. (1)] for the cylinder structure, a parametric angle  $\theta$  characterizing the coupling feature of the curved tube is introduced. By optimizing  $\theta$  the equivalence in the coupling properties between planar and curved tubes can be obtained (see Supplementary Fig. 5 of Supplementary Note 6), and one desired parametric angle is  $\theta = \pi/16$  (see Fig. 1d) for tube width  $d$  in the range of 1–4.5 mm (with tube length 9.3 mm) when the dimensions of acoustic resonator are as follows:  $a = 5.2$  mm,  $b = 10$  mm,  $c = 20$  mm.

In the measurement of half translation of edge bands, and BOTP and SPTP transitions, we compare the measured results with those of simulations, which are computed based on ribbon structure of resonator arrays. The ribbon structure has one unit cell along the periodic boundaries (for instance,  $x$  direction) that is accompanied with 'Floquet periodicity', that is, differing by a phase  $e^{ik_x a}$  ( $a$  is the lattice constant along  $x$ ), and 15 unit cells in the open boundaries. The edge band structure can be obtained by scanning  $k_x$  from  $-\pi$  to  $\pi$ . Similarly, to compare the measured bulk, edge, corner spectra, and the sound pressure distribution with those of simulation, we obtain the simulation results based on planar acoustic array with  $7 \times 7$  unit cells and full open boundary condition by computing the eigen frequencies and corresponding eigen wave functions.

### Data availability

The data underlying results presented in this paper are available from the corresponding author upon reasonable request.

### Code availability

The simulation and data processing codes that support the plots within this paper will be made available by the corresponding author upon reasonable request.

Received: 22 January 2025; Accepted: 3 July 2025;

Published online: 18 July 2025

### References

- Zhang, C., Chen, Z., Zhang, Z. & Zhao, Y. General theory of momentum-space nonsymmorphic symmetry. *Phys. Rev. Lett.* **130**, 256601 (2023).
- Chen, Z., Zhang, Z., Yang, S. A. & Zhao, Y. Classification of time-reversal-invariant crystals with gauge structures. *Nat. Commun.* **14**, 743 (2023).
- Zhao, Y., Chen, C., Sheng, X.-L. & Yang, S. A. Switching spinless and spinful topological phases with projective p t symmetry. *Phys. Rev. Lett.* **126**, 196402 (2021).
- Xue, H. et al. Stiefel-whitney topological charges in a three-dimensional acoustic nodal-line crystal. *Nat. Commun.* **14**, 4563 (2023).
- Meng, Y. et al. Spinful topological phases in acoustic crystals with projective p t symmetry. *Phys. Rev. Lett.* **130**, 026101 (2023).

6. Herzog-Arbeitman, J., Song, Z.-D., Elcoro, L. & Bernevig, B. A. Hofstadter topology with real space invariants and reentrant projective symmetries. *Phys. Rev. Lett.* **130**, 236601 (2023).
7. Liu, Z., Wei, G., Wu, H. & Xiao, J.-J. Möbius edge band and Weyl-like semimetal flat-band in topological photonic waveguide array by synthetic gauge flux. *Nanophotonics* **12**, 3481–3490 (2023).
8. Shiozaki, K., Sato, M. & Gomi, K. Z<sub>2</sub> topology in nonsymmorphic crystalline insulators: Möbius twist in surface states. *Phys. Rev. B* **91**, 155120 (2015).
9. Zhao, Y., Huang, Y.-X. & Yang, S. A. Z<sub>2</sub>-projective translational symmetry protected topological phases. *Phys. Rev. B* **102**, 161117 (2020).
10. Xue, H. et al. Projectively enriched symmetry and topology in acoustic crystals. *Phys. Rev. Lett.* **128**, 116802 (2022).
11. Li, T. et al. Acoustic möbius insulators from projective symmetry. *Phys. Rev. Lett.* **128**, 116803 (2022).
12. Long, Y. et al. Non-abelian braiding of topological edge bands. *Phys. Rev. Lett.* **132**, 236401 (2024).
13. Jiang, C., Song, Y., Li, X., Lu, P. & Ke, S. Photonic möbius topological insulator from projective symmetry in multiorbital waveguides. *Opt. Lett.* **48**, 2337–2340 (2023).
14. Chen, Z., Yang, S. A. & Zhao, Y. Brillouin Klein bottle from artificial gauge fields. *Nat. Commun.* **13**, 2215 (2022).
15. Tao, Y.-L. et al. Higher-order Klein bottle topological insulator in three-dimensional acoustic crystals. *Phys. Rev. B* **109**, 134107 (2024).
16. Zhu, Z. et al. Brillouin Klein space and half-turn space in three-dimensional acoustic crystals. *Sci. Bull.* (2024).
17. Li, C.-A., Sun, J., Zhang, S.-B., Guo, H. & Trauzettel, B. Klein-bottle quadrupole insulators and dirac semimetals. *Phys. Rev. B* **108**, 235412 (2023).
18. Li, T., Liu, L., Zhang, Q. & Qiu, C. Acoustic realization of projective mirror Chern insulators. *Commun. Phys.* **6**, 268 (2023).
19. Lu, L. et al. Symmetry-protected topological photonic crystal in three dimensions. *Nat. Phys.* **12**, 337–340 (2016).
20. Wang, Z., Alexandradinata, A., Cava, R. J. & Bernevig, B. A. Hourglass fermions. *Nature* **532**, 189–194 (2016).
21. Wang, R. et al. Symmetry-protected topological triangular Weyl complex. *Phys. Rev. Lett.* **124**, 105303 (2020).
22. Cheng, H., Sha, Y., Liu, R., Fang, C. & Lu, L. Discovering topological surface states of Dirac points. *Phys. Rev. Lett.* **124**, 104301 (2020).
23. Zhang, X. et al. Symmetry-protected hierarchy of anomalous multipole topological band gaps in nonsymmorphic metacrystals. *Nat. Commun.* **11**, 65 (2020).
24. Liu, Z., Wei, G. & Xiao, J.-J. Geometric anisotropy induced higher-order topological insulators in nonsymmorphic photonic crystals. *Phys. Rev. B* **106**, 085415 (2022).
25. Fonseca, A. G. et al. Weyl points on nonorientable manifolds. *Phys. Rev. Lett.* **132**, 266601 (2024).
26. Lv, B. et al. Experimental discovery of Weyl semimetal taas. *Phys. Rev. X* **5**, 031013 (2015).
27. Soluyanov, A. A. et al. Type-II Weyl semimetals. *Nature* **527**, 495–498 (2015).
28. Armitage, N., Mele, E. & Vishwanath, A. Weyl and Dirac semimetals in three-dimensional solids. *Rev. Mod. Phys.* **90**, 015001 (2018).
29. Wang, Z.-Y. et al. Realization of an ideal Weyl semimetal band in a quantum gas with 3d spin-orbit coupling. *Science* **372**, 271–276 (2021).
30. Hu, J., Zhuang, S. & Yang, Y. Higher-order topological insulators via momentum-space nonsymmorphic symmetries. *Phys. Rev. Lett.* **132**, 213801 (2024).
31. Resta, R. Theory of the electric polarization in crystals. *Ferroelectrics* **136**, 51–55 (1992).
32. King-Smith, R. & Vanderbilt, D. Theory of polarization of crystalline solids. *Phys. Rev. B* **47**, 1651 (1993).
33. Vanderbilt, D. *Berry phases in electronic structure theory: electric polarization, orbital magnetization and topological insulators* (Cambridge University Press, 2018).
34. Benalcazar, W. A., Bernevig, B. A. & Hughes, T. L. Quantized electric multipole insulators. *Science* **357**, 61–66 (2017).
35. Benalcazar, W. A., Bernevig, B. A. & Hughes, T. L. Electric multipole moments, topological multipole moment pumping, and chiral hinge states in crystalline insulators. *Phys. Rev. B* **96**, 245115 (2017).
36. Schindler, F. et al. Higher-order topological insulators. *Sci. Adv.* **4**, eaat0346 (2018).
37. Peterson, C. W., Benalcazar, W. A., Hughes, T. L. & Bahl, G. A quantized microwave quadrupole insulator with topologically protected corner states. *Nature* **555**, 346–350 (2018).
38. Mittal, S. et al. Photonic quadrupole topological phases. *Nat. Photonics* **13**, 692–696 (2019).
39. Qi, Y. et al. Acoustic realization of quadrupole topological insulators. *Phys. Rev. Lett.* **124**, 206601 (2020).
40. Ni, X., Li, M., Weiner, M., Alù, A. & Khanikaev, A. B. Demonstration of a quantized acoustic octupole topological insulator. *Nat. Commun.* **11**, 2108 (2020).
41. Xue, H. et al. Observation of an acoustic octupole topological insulator. *Nat. Commun.* **11**, 2442 (2020).
42. Serra-Garcia, M. et al. Observation of a phononic quadrupole topological insulator. *Nature* **555**, 342–345 (2018).
43. Imhof, S. et al. Topoelectrical-circuit realization of topological corner modes. *Nat. Phys.* **14**, 925–929 (2018).
44. Khalaf, E., Benalcazar, W. A., Hughes, T. L. & Queiroz, R. Boundary-obstructed topological phases. *Phys. Rev. Res.* **3**, 013239 (2021).
45. Geier, M., Trifunovic, L., Hoskam, M. & Brouwer, P. W. Second-order topological insulators and superconductors with an order-two crystalline symmetry. *Phys. Rev. B* **97**, 205135 (2018).
46. Queiroz, R., Fulga, I. C., Avraham, N., Beidenkopf, H. & Cano, J. Partial lattice defects in higher-order topological insulators. *Phys. Rev. Lett.* **123**, 266802 (2019).
47. Du, J., Li, T., Fan, X., Zhang, Q. & Qiu, C. Acoustic realization of surface-obstructed topological insulators. *Phys. Rev. Lett.* **128**, 224301 (2022).
48. Chen, J.-H. et al. Experimental realization of boundary-obstructed topological insulators using acoustic two-dimensional su–schrieffer–heeger network. *Appl. Phys. Lett.* **120**, 253508 (2022).
49. Lai, P. et al. Real-projective-plane hybrid-order topological insulator realized in phononic crystals. *Phys. Rev. Appl.* **21**, 044002 (2024).
50. Wang, Y. et al. Chess-board acoustic crystals with momentum-space nonsymmorphic symmetries. *arXiv preprint arXiv:2305.07174* (2023).
51. Tao, Y.-L., Wang, J.-H. & Xu, Y. Quadrupole insulator without corner states in the energy spectrum (2023). 2307.00486.
52. He, L., Addison, Z., Mele, E. J. & Zhen, B. Quadrupole topological photonic crystals. *Nat. Commun.* **11**, 3119 (2020).
53. Zhou, X. et al. Twisted quadrupole topological photonic crystals. *Laser Photonics Rev.* **14**, 2000010 (2020).
54. Lin, Z.-K., Wang, H.-X., Xiong, Z., Lu, M.-H. & Jiang, J.-H. Anomalous quadrupole topological insulators in two-dimensional nonsymmorphic sonic crystals. *Phys. Rev. B* **102**, 035105 (2020).
55. Zhou, P. et al. Realization of a quadrupole topological insulator phase in a gyromagnetic photonic crystal. *Natl. Sci. Rev.* nwae121 (2024).

## Acknowledgements

The authors thank Hengbin Cheng, André Grossi Fonseca, Yixin Sha, Sachin Vaidya, Yong Xu, Haoran Xue, and Mou Yan for fruitful discussions and Yangyang Zhao for experimental help. J. Hu acknowledges the support from the Natural Science Foundation of Shanghai (24ZR1453200), Y. Yang acknowledges the National Natural Science Foundation of China Excellent Young Scientists Fund (12222417), the Guangdong Provincial Quantum Science Strategic Initiative (GDZX2404005), the Hong Kong Research Grants Council through Early Career Scheme (27300924), Strategic Topics Grant (STG3/E-704/23-N), the Startup Fund of The University of Hong Kong, Ms. Belinda Hung, the Asian Young Scientist Fellowship, the Croucher Foundation, and New Cornerstone Science Foundation through the Explorer Prize.

### Author contributions

J. Hu, T. Song, and K. Zhou designed, built, and performed the measurement. J. Hu, T. Song, K. Zhou, and X. Jiang analyzed the data. J. Hu and Y. Yang developed the idea and wrote the manuscript with input from all authors. S. Zhuang and Y. Yang supervised the project. All authors contributed to the discussion of the results.

### Competing interests

The authors declare no competing interests.

### Additional information

**Supplementary information** The online version contains supplementary material available at <https://doi.org/10.1038/s42005-025-02218-7>.

**Correspondence** and requests for materials should be addressed to Jinbing Hu or Yi Yang.

**Peer review information** *Communications Physics* thanks the anonymous reviewers for their contribution to the peer review of this work.

**Reprints and permissions information** is available at <http://www.nature.com/reprints>

**Publisher's note** Springer Nature remains neutral with regard to jurisdictional claims in published maps and institutional affiliations.

**Open Access** This article is licensed under a Creative Commons Attribution-NonCommercial-NoDerivatives 4.0 International License, which permits any non-commercial use, sharing, distribution and reproduction in any medium or format, as long as you give appropriate credit to the original author(s) and the source, provide a link to the Creative Commons licence, and indicate if you modified the licensed material. You do not have permission under this licence to share adapted material derived from this article or parts of it. The images or other third party material in this article are included in the article's Creative Commons licence, unless indicated otherwise in a credit line to the material. If material is not included in the article's Creative Commons licence and your intended use is not permitted by statutory regulation or exceeds the permitted use, you will need to obtain permission directly from the copyright holder. To view a copy of this licence, visit <http://creativecommons.org/licenses/by-nc-nd/4.0/>.

© The Author(s) 2025